Volume 11 | Number 10 | 14 March 2015 | Pages 1853–2056

Soft Matter

www.softmatter.org

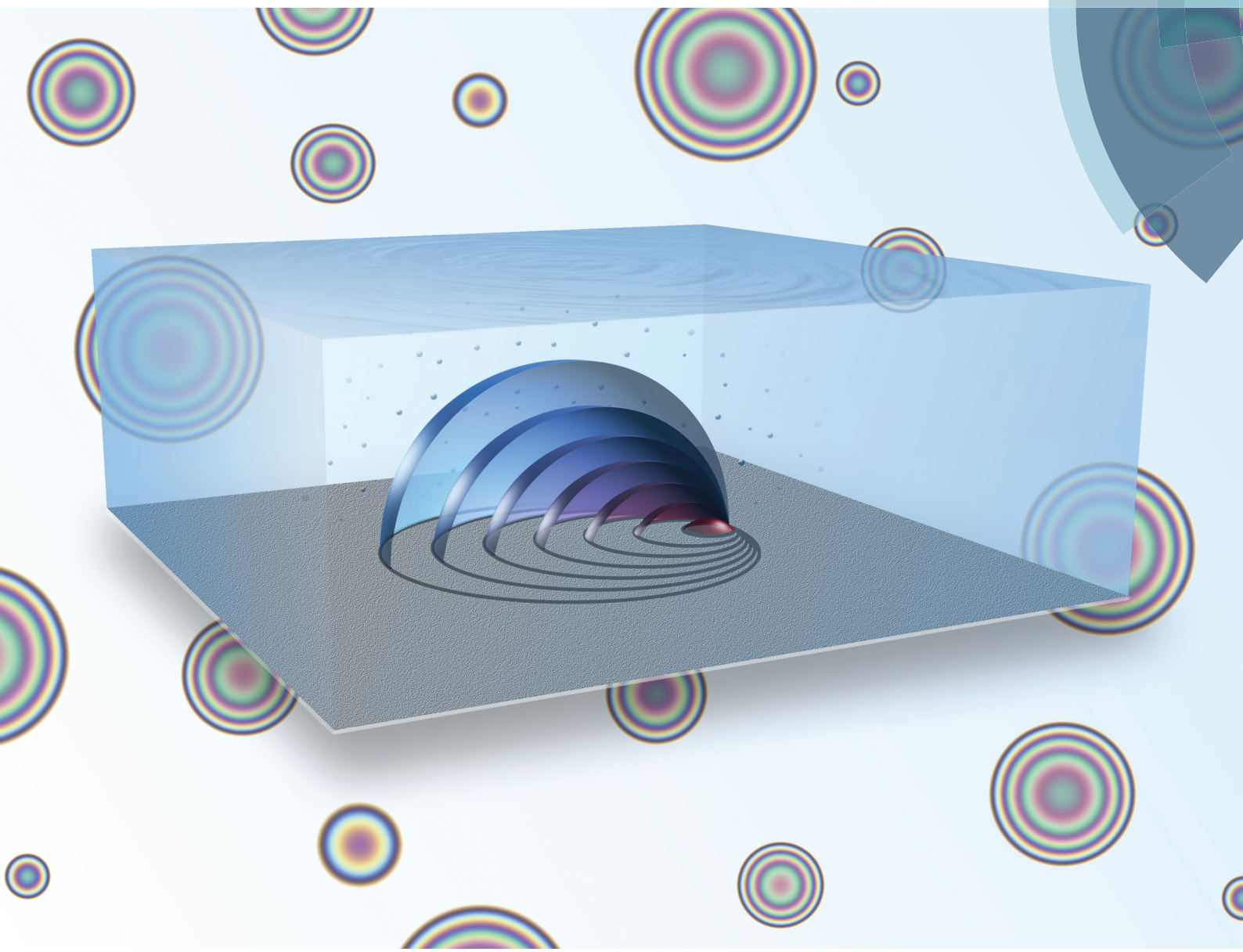

ISSN 1744-683X

ROYAL SOCIETY OF CHEMISTRY

PAPER
Xuehua Zhang *et al.*
Mixed mode of dissolving immersed nanodroplets at a solid–water interface

Soft Matter

PAPER

View Article Online
View Journal | View Issue

CrossMark click for updates

Cite this: *Soft Matter*, 2015, **11**, 1889

Mixed mode of dissolving immersed nanodroplets at a solid–water interface†

Xuehua Zhang,*[ab] Jun Wang,‡[b] Lei Bao,‡[a] Erik Dietrich,[bc] Roeland C. A. van der Veen,[b] Shuhua Peng,[a] James Friend,[d] Harold J. W. Zandvliet,[c] Leslie Yeo[a] and Detlef Lohse[b]

Received 31st October 2014
Accepted 5th January 2015

DOI: 10.1039/c4sm02397h

www.rsc.org/softmatter

The dissolution dynamics of microscopic oil droplets (less than 1 μm in height, *i.e.* nanodroplets) on a hydrophobilized silicon surface in water was experimentally studied. The lateral diameter was monitored using confocal microscopy, whereas the contact angle was measured by (disruptive) droplet polymerisation of the droplet. In general, we observed the droplets to dissolve in a mixed mode, *i.e.*, neither in the constant contact angle mode nor in the constant contact radius mode. This means that both the lateral diameter and the contact angle of the nanodroplets decrease during the dissolution process. On average, the dissolution rate is faster for droplets with larger initial size. Droplets with the same initial size can, however, possess different dissolution rates. We ascribe the non-universal dissolution rates to chemical and geometric surface heterogeneities (that lead to contact line pinning) and cooperative effects from the mass exchange among neighbouring droplets.

Published on 06 January 2015. Downloaded on 03/03/2015 10:50:05.

Introduction

Submicron surface droplets – also called surface nanodroplets – refer to droplets at a solid–liquid interface that have at least one dimension less than 1 μm. Those droplets are important in various chemical and environmental processes, such as in oil-assisted mineral flotation, oil spill clean-up, or droplet-templated porous materials. They are also highly relevant to fluid transport in microfluidics for applications across chemical synthesis and biomedical diagnosis, amongst others.[1–4]

Very similar to surface nanodroplets are surface nanobubbles, *i.e.*, microscopic bubbles at solid–liquid interface.[5–12] An intriguing property of surface nanobubbles is their very long lifetime up to days. The mechanism for the nanobubble stability has been highly controversial. We think that the crucial mechanisms contributing to the long lifetime of surface nanobubbles are contact line pinning and collective effects that arise from neighbouring nanobubbles.[13–15] Quantitative experiments to probe the lifetime of these bubbles and thus their dissolution behavior are however difficult for surface nanobubbles as it is highly non-trivial to control the exact gas saturation level which of course plays a crucial role for the bubble lifetime.

The theoretical framework to understand the dissolution behavior of surface nanobubbles is equally applicable to surface nanodroplets. The big advantage of nanodroplet dissolution experiments as compared to surface nanobubble dissolution studies is that the solvent concentration can be much easier controlled and that the lifetime can be tuned more easily by choosing a solvent with appropriate solubility, thus setting the timescale of the process to an appropriate value, allowing for detailed tracking of the surface nanodroplet dissolution dynamics.

This is what we will show in the present work, *i.e.*, we will present our experimental results from dissolution studies of surface nanodroplets. The formation of surface nanodroplets was achieved through solvent exchange,[16–18] akin to that employed to generate surface nanobubbles.[19–21] The morphology of the droplets was subsequently characterised by polymerising them to permanent stable microstructures,[17,18,22] which are often referred to as lenses because of their lens-like shape.[16–18] In particular, we examined their lateral diameter using confocal microscopy imaging and the contact angle by polymerising droplets at different times. The results show that those droplets shrank both in lateral diameter and in height during the dissolution, confirming that the pinning of the nanodroplet boundary plays an important role, giving rise to a *mixed* dissolution mode, *i.e.*, neither the constant contact angle mode nor the constant contact radius mode.

[a]*School of Civil, Environmental and Chemical Engineering, RMIT University, Melbourne, VIC 3001, Australia. E-mail: xuehua.zhang@rmit.edu.au*

[b]*Physics of Fluids Group, Department of Applied Physics and J. M. Burgers Centre for Fluid Dynamics, University of Twente, P. O. Box 217, 7500 AE Enschede, The Netherlands*

[c]*Physics of Interfaces and Nanomaterials, MESA+ Institute for Nanotechnology, University of Twente, P. O. Box 217, 7500 AE Enschede, The Netherlands*

[d]*School of Electrical and Computer Engineering, RMIT University, Melbourne, VIC 3001, Australia*

† Electronic supplementary information (ESI) available: Data pertaining to the reconstructed profiles and contact angle of nanodroplets in MMA-saturated water. Also provided are the lateral diameter of the different nanodroplets shown in the confocal microscopy images as a function of time and optical images of decane under water in a flow condition. See DOI: 10.1039/c4sm02397h

‡ JW and LB contributed equally.

Published on 06 January 2015. Downloaded on 03/03/2015 10:50:05.

Theoretical analysis of a dissolving droplet

A sketch of a surface droplet, including our notation, is shown in Fig. 1. The droplet volume

$$V = \pi H(3L^2 + 4H^2)/24 \quad (1)$$

follows from the droplet height H and the lateral diameter L. The contact angle θ expressed in terms of these quantities reads

$$\sin\theta = \frac{4LH}{L^2 + 4H^2}. \quad (2)$$

In the quasi-steady limit, the diffusion of the solute in the solvent is the rate-limiting mechanism, which is the relevant case for dissolution in still water. In this limit, the diffusion equation governing the transport of a species with a concentration field $c(r, z)$ around the droplet is then the diffusion equation

$$\partial_t c = D\nabla^2 c \approx 0, \quad (3)$$

where r and z are the radial and vertical coordinates, respectively, and D is the diffusion constant. At the droplet–water interface, the solvent concentration equals the saturation concentration c_s. Far away from the droplet $c(z \to \infty) = c(z \to \infty) = c_\infty$, whereas the no-flux condition $\partial c/\partial z = 0$ applies on the substrate surface $z = 0$. The diffusive flux can also be specified by Fick's law: $J = -D\nabla c$.

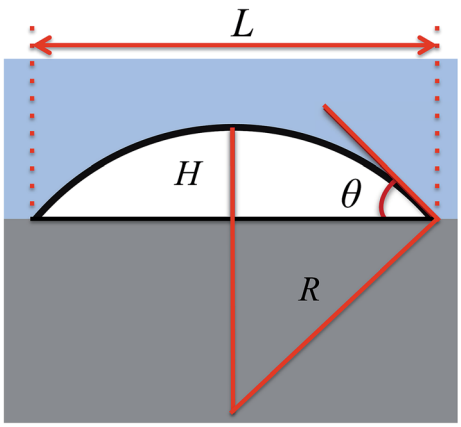

Fig. 1 Sketch and notation of a surface droplet. L is the lateral diameter, θ the contact angle, H the maximum height of the droplet, and R the radius of curvature.

The approximate droplet dissolution in the small contact angle limit was calculated by (ref. 23 and 24). The full problem for any contact angle was solved by (ref. 25), using an elegant analogy to the electric potential around a charged lens-shaped conductor. The mass loss dM/dt of a droplet is[25,26]

$$\frac{dM}{dt} = -\frac{\pi}{2}LD(c_s - c_\infty)f(\theta) \quad (4)$$

where

$$f(\theta) = \frac{\sin\theta}{1+\cos\theta} + 4\int_0^\infty \frac{1+\cosh 2\theta\xi}{\sinh 2\pi\xi}\tanh[(\pi-\theta)\xi]d\xi. \quad (5)$$

Given the density ρ the mass M of the droplet can then be expressed in terms of the lateral diameter L and the contact angle θ as

$$M(\theta) = \rho\frac{\pi}{8}L^3\frac{\cos^3\theta - 3\cos\theta + 2}{3\sin^3\theta} = \rho\frac{\pi}{8}L^3 g(\theta). \quad (6)$$

From eqn (4) and (6) we can read off (apart from the prefactor 8, which we introduce for later convenience) the time scale $\tau(L)$ of the dissolution process of a droplet of lateral extension L, namely,

$$\tau(L) = \frac{L^2\rho}{8Dc_s}. \quad (7)$$

In Table 1 we give the material properties of the three droplet liquids employed in this study and the resulting dissolution time scales. Further quantities determining the dissolution time are the contact angle θ and the undersaturation

$$\zeta = 1 - c_\infty/c_s, \quad (8)$$

with the maximum $\zeta = 1$ for pure water $c_\infty = 0$, with $\zeta = 0$ for full saturation $c_\infty = c_s$, and $\zeta < 0$ for oversaturation (which we do not consider here).

The above dynamical equations can be analytically solved for two limiting cases,[27] namely for the constant contact angle mode ('CA' for constant angle, Fig. 2b) and for the constant contact area mode ('CR' for constant contact radius, Fig. 2a).

(i) *CR-mode*, *i.e.* pinned contact line and thus fixed L:
Eqn (4)–(6) then reduce to

Table 1 Material properties of the analysed droplets and the resulting time scale $\tau = \frac{L^2\rho}{8Dc_s}$ for a typical droplet with lateral extension $L = 10$ μmm. Here c_s is the oil solubility in water, ρ is the droplet density, and D the diffusion constant

Droplet liquid	$\frac{c_s}{kg/m^3}$	$\frac{\rho}{kg/m^3}$	$\frac{D}{m^2/s}$	$\frac{\tau(L=10\ \mu m)}{s}$
Methyl methacrylate (MMA)	15	936	8.8×10^{-10}	0.9
1,6-Hexanediol diacrylate (HDODA)	0.343	1202	6.5×10^{-10}	68
n-Decane	5.2×10^{-5}	730	7.5×10^{-10}	2.4×10^5

This journal is © The Royal Society of Chemistry 2015

Published on 06 January 2015. Downloaded on 03/03/2015 10:50:05.

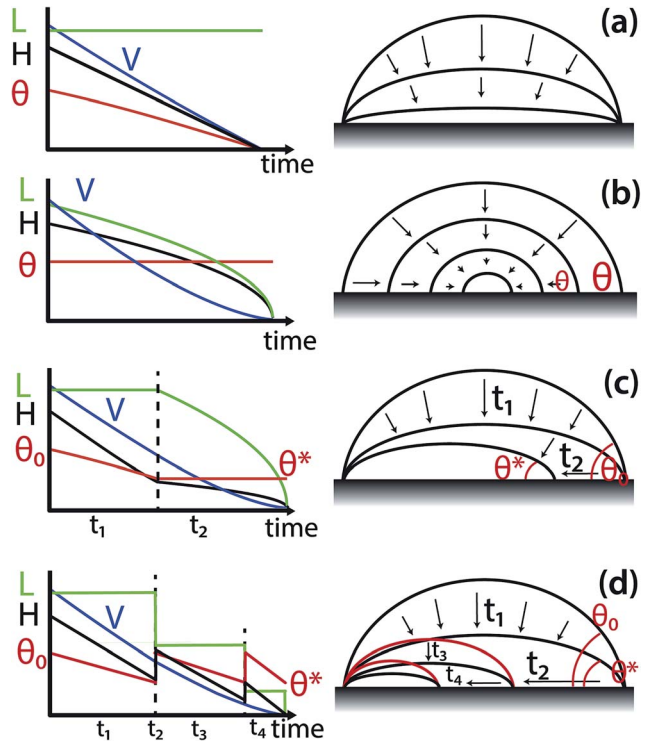

Fig. 2 Schemes of the four possible dissolution modes of a surface nanodroplet (or a surface nanobubbles): (a) CR-mode, *i.e.*, constant contact radius due to perfect pinning. (b) CA-mode, *i.e.*, constant contact angle. (c) Stick–slide (SS) mode, *i.e.* the nanodroplet dissolves in an iteration of the CR and the CA modes. (d) Jumping-mode. The droplet first is in a CR mode, but for an angle smaller than θ^* jumps towards a smaller constant radius due to sudden depinning on one side. Due to mass conservation at the jump the droplet height and contact angle jump up. After the jump, the droplet is again in a CR mode, up to the next jump, finally resulting in a cascade of jumps (not drawn).

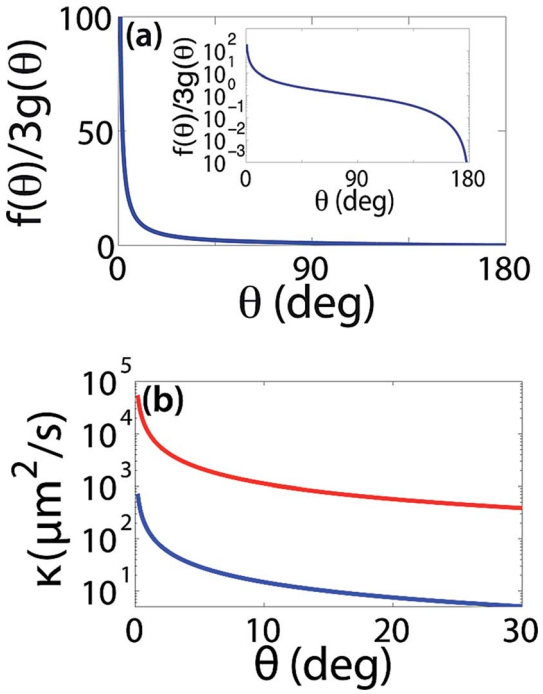

Fig. 3 (a) Wall correction factor $f(\theta)/(3g(\theta))$, representing the modification of the dissolution time scale of a hemispherical droplet with constant contact angle θ at a wall as compared to an individual spherical droplet in the bulk. For $\theta = 90°$ this correction factor is 1. The inset shows the same, but now with the correction factor on a logarithmic scale. (b) The theoretical dissolution rates $\kappa(\theta)$ for MMA (red curve) and HDODA (blue curve), assuming dissolution with constant contact angle θ throughout the dissolution (pure CA-mode). The curves are obtained from eqn (15) with the material parameters from Table 1, assuming dissolution in pure water ($\zeta = 1$). As one can see, the dissolution rate of MMA is two orders of magnitude larger than that of HDODA.

$$\frac{\mathrm{d}\theta}{\mathrm{d}t} = -\frac{4D(c_s - c_\infty)}{\rho L^2}(1+\cos\theta)^2 f(\theta). \tag{9}$$

This equation can easily be solved by numerical integration and, for the case of an evaporating pinned droplet in still ambient air, the result gives excellent agreement with experimental data.[26,28] Here we numerically integrate eqn (9) for a MMA droplet in pure water ($c_\infty = 0$) with (constant) $L = 10$ μm and initial contact angle $\theta_0 = 30°$. From the resulting $\theta(t)$ and eqn (1) and (2) we finally obtain the time evolution of the volume $V(t)$ in this assumed CR mode, see Fig. 4d. We also obtain the lifetime of about 0.25 s.

(ii) *CA-mode*, *i.e.*, constant contact angle θ:

We then obtain

$$L\dot{L} = \frac{4(c_s - c_\infty)D}{\rho}\frac{f(\theta)}{3g(\theta)} \tag{10}$$

which can be integrated to obtain a relationship that describes the time evolution of the lateral diameter of the dissolving droplet with constant contact angle θ:

$$L(t) = \left(L_0^2 - \frac{8(c_s - c_\infty)D}{\rho}\frac{f(\theta)}{3g(\theta)}t\right)^{1/2} \tag{11}$$

Note that apart from the wall correction factor $f(\theta)/(3g(\theta))$ this is the same result as for the dissolution of an individual spherical droplet or bubble with diameter $L(t)$ in the bulk, as first derived by Epstein and Plesset.[29]

Eqn (11) can be rewritten as

$$\frac{L^2(t)}{L_0^2} = 1 - \frac{t}{t_{\mathrm{diss}}} \tag{12}$$

with the dissolution time

$$t_{\mathrm{diss}} = \frac{L_0^2\rho}{8D(c_s - c_\infty)}\frac{3g(\theta)}{f(\theta)} = \tau(L_0)\frac{1}{\zeta}\frac{3g(\theta)}{f(\theta)} \tag{13}$$

As seen from eqn (13), the dissolution time quadratically depends on the initial lateral droplet extension L_0, as expected already from eqn (7). Therefore, to better work out the universality, we rewrite eqn (11) or (12) as

Published on 06 January 2015. Downloaded on 03/03/2015 10:50:05.

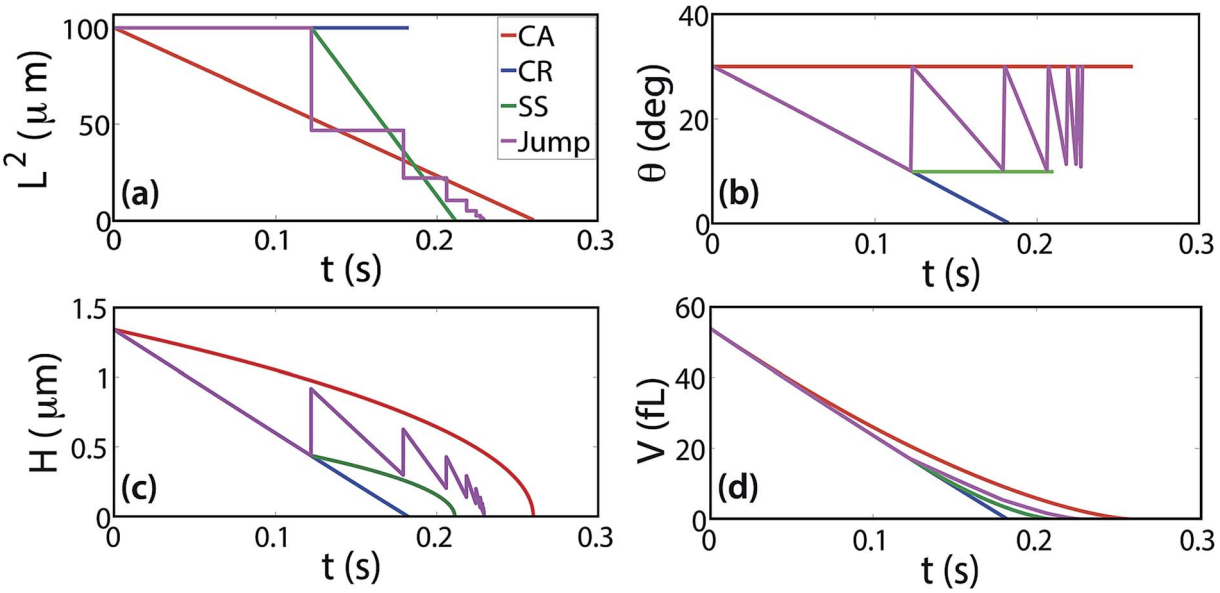

Fig. 4 Time evolution of various characteristic quantities of a dissolving MMA droplet in pure water ($\zeta = 1$) with initial lateral extension $L = 10$ μm and initial contact angle $\theta = 30°$ when dissolving in the four modes CR, CR, stick–slide (SS), and jumping. For this latter case we assumed that the jumping occurs at $\theta^* = 10°$. (a) Lateral diameter square L^2. (b) Contact angle θ. (c) Maximal droplet height H. (d) Droplet volume $V = \pi H(3L^2 + 4H^2)/24$.

$$L^2(t) = {L_0}^2 - \frac{8Dc_s\zeta}{\rho}\frac{f(\theta)}{3g(\theta)}t =: {L_0}^2 - \kappa(\theta)t. \qquad (14)$$

In a plot of $L^2(t)$ *vs.* time t the slope (*i.e.*, the dissolution rate)

$$\kappa(\theta) := \frac{8Dc_s\zeta}{\rho}\frac{f(\theta)}{3g(\theta)} = \frac{{L_0}^2}{\tau(L_0)}\zeta\frac{f(\theta)}{3g(\theta)} = \frac{{L_0}^2}{t_{\mathrm{diss}}(L_0)}, \qquad (15)$$

which carries the dimensions of an diffusion constant (*i.e.*, $m^2\ s^{-1}$) and which can easily be extracted, now only depends on the contact angle θ. If θ were constant and the same for all droplets (*i.e.*, pure CA-mode for all droplets), the slope of the curves should be universal. In the experimental part of the paper, we will use such plots of $L^2(t)$ *vs.* t to extract κ for the various droplets we will analyse.

We now discuss the wall correction factor in more detail. It is plotted in Fig. 3a, both on a linear and on a log scale. As expected, for $\theta = 90°$ it equals 1, implying that the dissolution of a hemispherical droplet is identical to that of a spherical droplet, due to the 'image' of the hemispherical droplet, with together with the hemispherical droplet itself is spherical. For smaller $\theta < 90°$ the dissolution is enhanced, as then $f(\theta)/(3g(\theta))$ and thus $\kappa(\theta)$ becomes larger than 1, whereas for larger $\theta > 90°$ the dissolution is delayed. As seen from Fig. 3a, this angular effect can be considerable. Fig. 3b shows the resulting contact angle dependence of the theoretical dissolution rates $\kappa(\theta)$ for MMA and HDODA, assuming dissolution with constant contact angle (CA-mode).

In Fig. 4d we plotted the time dependence of the volume $V(t)$ for a MMA surface nanodroplet of initial lateral extension $L = 10$ μm in pure water ($\zeta = 1$), dissolving in the CA-mode (for $\theta = 30°$) and compare it to above calculated dissolution in the CR mode. The droplet lifetime is about 0.25 s in the CA mode and about 0.18 s in a CR mode.

In general, it must be expected that the droplets dissolve in a combined CR–CA mode. This could be the so-called 'stick–slide' (SS) mode,[30,31] comprising the two limiting cases in alternate succession, as sketched in Fig. 2c. Interestingly, the lifetime of a droplet in such a general mode is not constrained by the lifetimes of the limiting cases, but can be larger.[31] A fourth dissolution mode is what we call the jumping-mode, see Fig. 2d: it also is a combined CR–CA mode, starting with constant contact radius due to pinning. Here the height H and thus the contact angle θ shrink. Once the contact line suddenly depins on one side, the contact radius jumps towards a smaller value, implying an *upwards* jump in the height H and in the contact angle θ, due to mass ($\propto L^2H$) conservation at the jump.

The dissolution dynamics for MMA droplets in the four dissolution modes is compared in Fig. 4.

Experimental section

1. Chemicals and surface preparation

Octadecyltrimethylchlorosilane (OTS, >90%), methyl methacrylate (MMA, 99%), 1,6-hexanediol diacrylate (HDODA), and a photo-initiator (2-hydroxy-2-methylpropiophenone) were purchased from Sigma-Aldrich (U.S.). Toluene (AR), chloroform (AR), ethanol (absolute, 100%) and *n*-decane (anhydrous, 99%) were supplied by Merck Pty Ltd (Australia). All chemicals were used as received unless otherwise specified. Single-sided polished silicon wafers were acquired from Mitsubishi Silicon (U.S.) and cover glasses from Menzel-Gläser (Germany).

OTS coated silicon wafers/glasses were used as the hydrophobic substrates in the formation of the submicron surface droplets. The silicon wafers or glasses were first immersed into freshly prepared Piranha solution (70% H_2SO_4–30% H_2O_2) at 70 °C for 30 min, then rinsed with Milli-Q water and dried in an

 This journal is © The Royal Society of Chemistry 2015

Published on 06 January 2015. Downloaded on 03/03/2015 10:50:05.

oven at 120 °C for 2 h. The dry substrates were immediately immersed in 0.5 vol% OTS in toluene solution inside a sealed container. After 12 h, the OTS-coated substrates were taken out, rinsed with chloroform and toluene subsequentially, and then dried.

In the formation of MMA nanodroplets, solution A consisted of a the monomer mixture of 90% methyl methacrylate (MMA) and 10% 1,6-hexanediol dimethacrylate (HDODA). 0.16 mL of the monomer mixture was added into 10 mL of 50% ethanol aqueous solution to obtain saturation of monomer in solution A. The same monomer mixture was used to prepare solution B, which comprised the monomer-saturated water. The nanodroplets that precipitate out from the solutions should therefore consist of mainly MMA with a small fraction of HDODA. nanodroplets of HDODA or decane, on the other hand, were produced by using their saturated solution A and B. To aid visualisation, the nanodroplets were fluorescently dyed using the Rhodamine 6G dissolved in the monomer at a concentration of 5 μM for the solvent exchange. It is impossible to provide the exact chemical composition of the droplets. However, the compositions are expected to be same for all droplets, because those monomers are highly soluble in each other. The dye is highly soluble in the monomer solution, too. So no segregation effects can be expected.

2. Formation and dissolution of nanodroplets

To form the nanodroplets on OTS-Si substrates, the solvent exchange was performed in a custom-made fluid cell with OTS-Si substrates fixed to the bottom of the cell. Briefly the solution A was first injected into the cell, followed by solution B in exchange for solution A at a fluid rate of 0.2 mL min^{-1}, which then led to the formation of surface droplets. The schematic drawing of the fluid cell was shown in our previous publications[16,17,32] and we do not reproduce it here.

To measure the dissolution rate, the monomer-saturated water in contact with the nanodroplets was gradually replaced with pure water. We examine two scenarios. In one set of experiments, the water was kept stationary, and any perturbation to the system was carefully avoided. In the other set of experiments, pure water was flushed continuously over the nanodroplets at a flow rate of 0.2 mL min^{-1}. Confocal images of the nanodroplets (see below) were then collected at different times to obtain information on the evolution of their lateral diameter during their dissolution.

To measure the height and hence contact angle of the nanodroplets, we added a photoinitiator to solution B, followed by UV cross linking after the nanodroplets were formed. The polymerisation conditions (UV intensity, duration *etc.*) were identical in all the experiments. The substrate with the polymerised nanodroplets (*i.e.*, the microlenses) was then removed from the fluid cell for further characterisation. In the dissolution experiments, the HDODA nanodroplets were polymerised after 5 min, 10 min and 20 min in a flow of pure water. Our measurements showed that the contact angle of the droplets decreased by approximately 1° after the polymerisation due to the density difference between its monomer and the polymer.

Table 2 Overview on the nine analysed cases in this paper. The various cases are given numbers for easy reference

Droplet liquid	$\tau(L = 10\ \mu m)$ / s	Saturated	Initially clean	Continuously refreshing
MMA	0.9	Case 1	Case 2	Case 3
HDODA	68	Case 4	Case 5	Case 6
n-Decane	2.4×10^5	Case 7	Case 8	Case 9

3. Characterisation of liquid and polymerised nanodroplets

Laser scanning confocal microscopy (LSCM, N-STORM, Nikon) was used to obtain the bottom view of liquid nanodroplets. As the LSCM only needs a very short scanning time, high contrast images can be obtained through point illumination using a green laser and out-of-focus light elimination by a spatial pinhole.

The LSCM images were post processed by loading them in to a custom-written Matlab program. The bright spots in the images, representing the droplets, were automatically detected and measured to extract the footprint diameter (*i.e.* lateral diameter, L) of the droplets. All droplets were tracked throughout the image sequence, so that the size evolution of each droplet in time could be followed. Only those droplets that could live long enough and be detected in the first four frames were considered for analysis. Dissolution rates were measured by plotting the squared footprint diameter in time. A straight line was fitted to these points using a least square method.

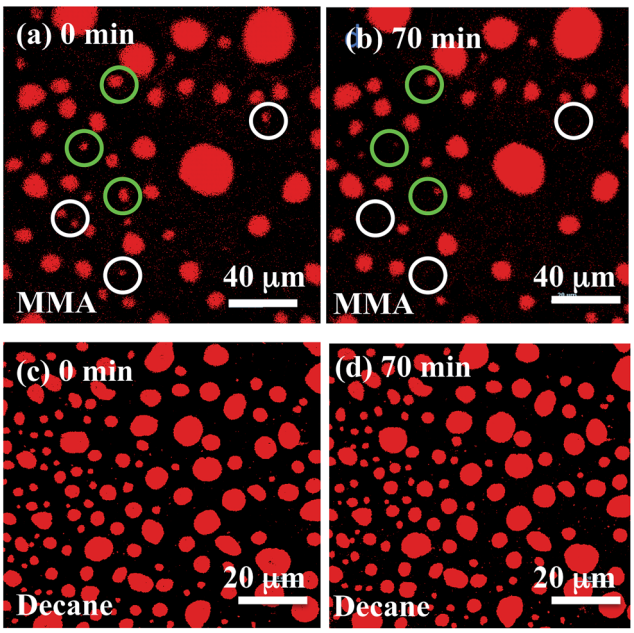

Fig. 5 Confocal microscopy images of (a and b) MMA (case 1) and (c and d) decane (case 7) surface nanodroplets in saturated water. The lateral diameter of MMA nanodroplets in (a) are observed to change over time, as seen after 70 min in (b). For example, MMA nanodroplets can be seen to shrink (green circles) or even to disappear completely (white circles). On the other hand, there is little change observed in the size of decane nanodroplets in (c), even after 70 min, as seen in (d).

Published on 06 January 2015. Downloaded on 03/03/2015 10:50:05.

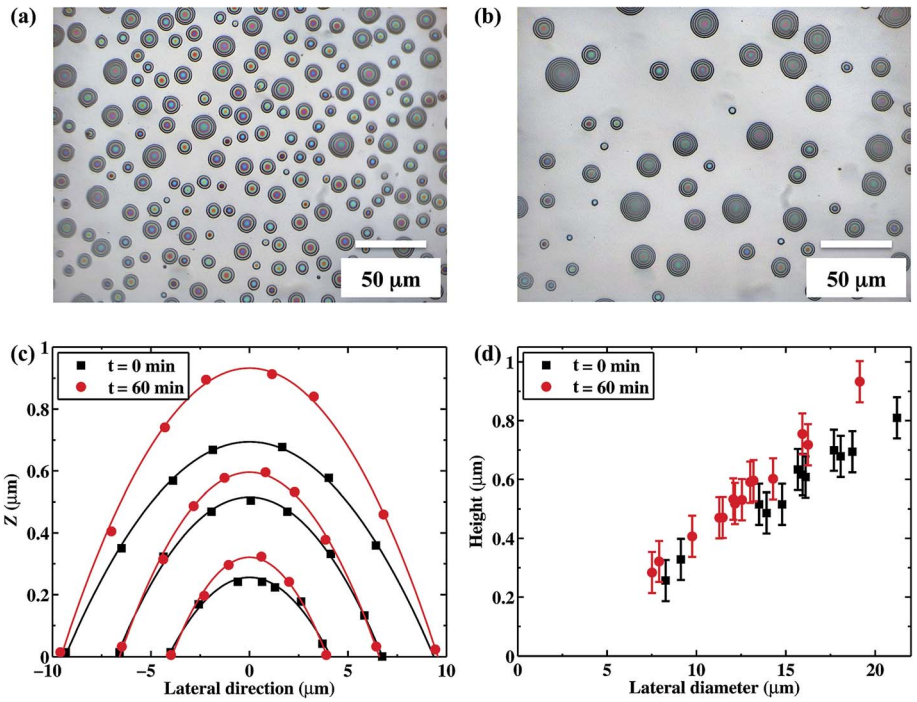

Fig. 6 Morphology of the PMMA microlenses. (a) and (b) are reflection mode optical images from nanodroplets polymerised (a) immediately, or (b) 60 min after their formation. (c) Representative reconstructed cross-sectional profiles, determined from the color and spacing of Newton rings from the blowups in (a) and (b). The axis Z is the distance from the lens surface to the substrate. (d) The maximum lens height *versus* lateral diameter of microlenses. The uncertainty in height is 70 nm, determined by limitation of the technique.

Images of the polymerised nanodroplets, on the other hand, were acquired using a reflection-mode optical microscopy. The interference pattern due to the reflection between the lens' surface and the underlying non-transparent substrate was then used to extract the morphological characteristics of those microlenses. More specifically, the profile of the microlens can be reconstructed from the color and the spacing of the rings in the reflection mode image *via* the image processing.[33] This method relies on a color-matching approach in combination with known reference surfaces. The inclusion of a non-unity refractive index in the analysis is required. Refractive indices of 1.491 for the PMMA lenses and 1 for the surrounding air medium are used. The uncertainty in the height is ±140 nm, with an intrinsic part of 40 nm in the reference color database[33] and 100 nm due to differences in *e.g.* the white balance and exposure between the measurements and reference images.

High resolution images of the microlenses were also obtained from normal contact mode AFM imaging. In particular, the morphology of the polymerized droplets were imaged in air by using the contact mode of a MFP-3D atomic force microscope (Asylum Research, Santa Barbara, CA), from whose topography images allowed the reconstruction of the height, lateral size and cross-sectional profiles of the polymerized droplets.

4. Explored cases

We did experiments with three different droplet liquids whose material properties are given in Table 1. They have very different solubilities, to be able to explore different time regimes. These are indicated by giving the time scale $\tau(L = 10\ \mu m)$ for a $L = 10$ μm nanodroplet. In addition, we employ three different flow conditions: droplets in saturated water, droplets in initially fresh water (which will be 'contaminated' by the droplet liquid during the dissolution process), and droplets in fresh and continuously renewed water, which will guarantee $c_\infty = 0$ for all time, apart from transients in the beginning of the exchange process. The nine cases are summarised in Table 2 and given numbers for easy reference.

Results and discussion

1. Stable droplets

We first show results for case 1, *i.e.*, MMA droplets in saturated water. Fig. 5a and b are confocal microscopy images, demonstrating that the lateral diameter of the MMA droplets was non-uniform, ranging from 1.5 μm to 11 μm. It is possible that smaller droplets may also be formed but were beyond the confocal resolution limit. It can be observed that even though many droplets remained on the surface even after 70 min in the MMA-saturated water, some small droplets were observed to have shrunk or even completely dissolved. With this method, no growth of any droplets could be detected.

In contrast, decane nanodroplets in saturated solution (case 7) with lateral diameters between 1.5 μm and 10 μm were observed to remain fairly stable even after 70 min in decane-saturated water (Fig. 5c and d). This clearly indicates that decane nanodroplets possess superior stability compared to

 This journal is © The Royal Society of Chemistry 2015

Published on 06 January 2015. Downloaded on 03/03/2015 10:50:05.

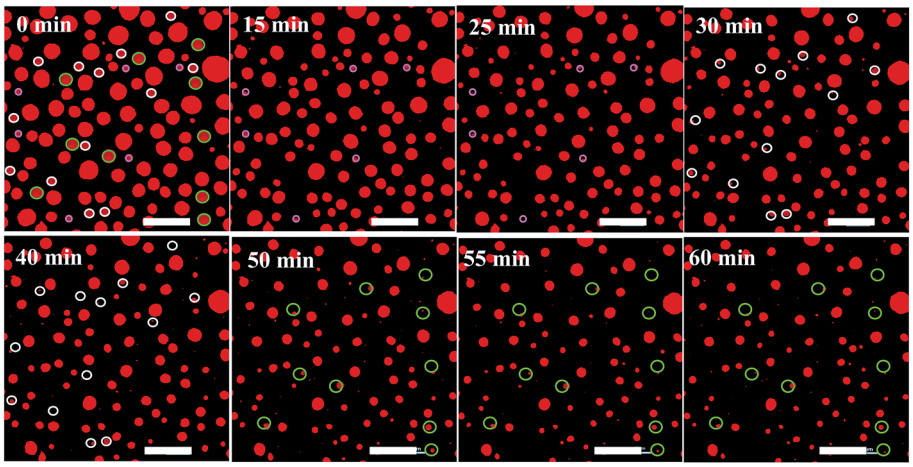

Fig. 7 Confocal microscopy snapshots of MMA nanodroplets at different times in still initially clean water (case 2). The circles are placed at identical locations in all the images with different colors indicating the droplets with different initial sizes. The diameters of the circles are 5 μm (pink), 8 μm (white), and 12 μm (green). Scale bar: 40 μm.

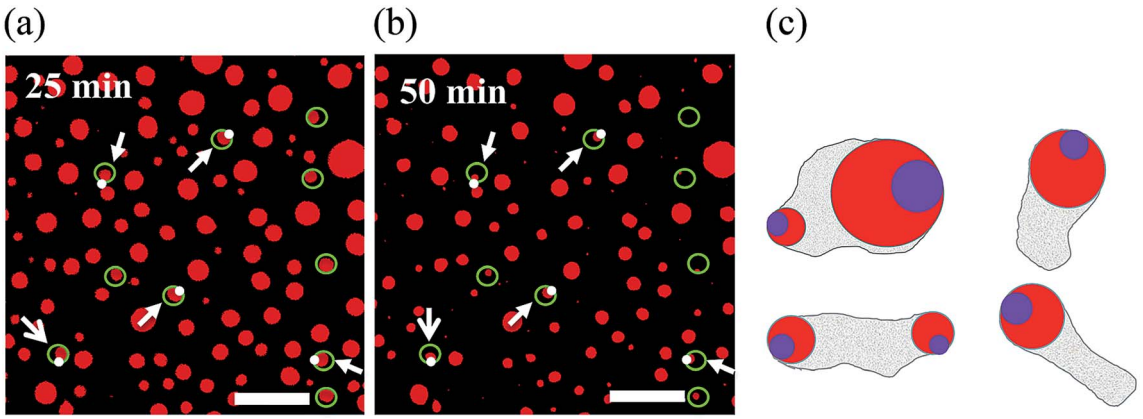

Fig. 8 Confocal microscopy images of dissolving MMA nanodroplets (case 2), highlighting the effect of pinning. (a) $t = 25$ min after the liquid exchange. (b) $t = 50$ min after the liquid exchange. Green circles and white dots are placed on the same location in two images. The arrows point to the directions of the shrinkage and the white dots indicate the pinning points. Length of the scale bar: 40 μm. (c) The sketch shows the top-view of patches of chemical heterogeneities (grey) with more hydrophobicity, where droplets (red) sit. During the dissolution, the boundary is pinned and the droplets jump towards a smaller footprint, as drawn by the smaller purple circles.

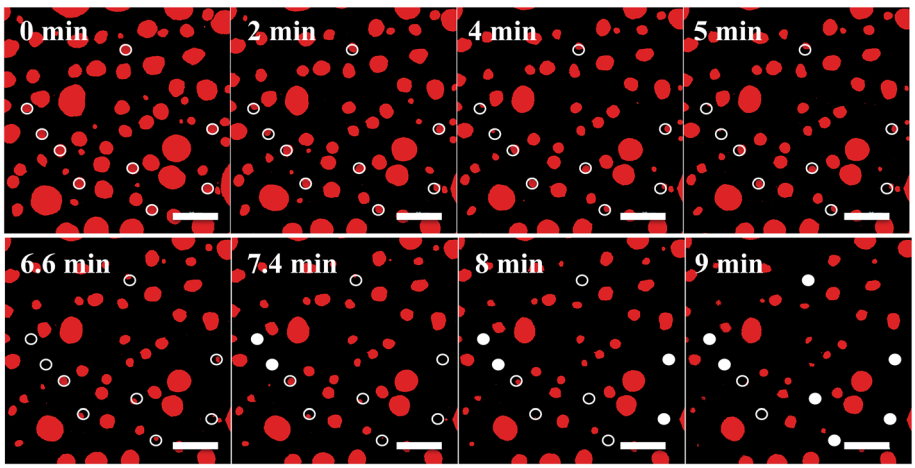

Fig. 9 Confocal microscopy images of MMA nanodroplets at different times under the flow of pure water (case 3). The open circles indicate identical locations in all images with a diameter of 12 μm, whereas the filled circles that were added indicate the disappearance of the droplets in the previous frame. Length of the scale bar: 40 μm.

Published on 06 January 2015. Downloaded on 03/03/2015 10:50:05.

their MMA counterparts. This can be explained by the much lower solubility of decane in water compared to that for MMA, leading to a time scale which is more than five orders of magnitude larger, see Table 1.

The PMMA lenses which formed from the polymerisation of the MMA nanodroplets in MMA-saturated water (case 1), either immediately after their formation or 60 min later, are shown in Fig. 6. The circular Newton rings on the PMMA microlenses allowed for the reconstruction of their cross-sectional profiles *via* image processing and hence the estimation of their height. All of the reconstructed profiles are provided in the ESI.† The ratio of height and lateral size of nanodroplets became slightly larger after 60 min, as shown in Fig. 6c and d. Together with the observation of Fig. 5 that some small droplets shrink or vanish, this suggests some Ostwald ripening type process for this saturated liquid case: an expansion in the volume of larger droplets with time at expense of smaller droplets. Note that we expect such ripening process to go on also in case 7, but due to the low solubility of decane it takes way too long to be observable in reasonable time. Below we will discuss Ostwald ripening in more detail.

2. Dissolving droplets

We now come to the case of dissolving droplets, *i.e.*, the surrounding water was slowly (on a time scale of two minutes for the exchange of the full volume) replaced by a flow of pure water. Note that we do not stir the liquid and the Peclet number is thus much smaller than 1. Therefore the mass transfer is determined by the diffusion equation, without any contribution from convection. The dissolution of MMA nanodroplets was tracked under both static and slow flow conditions of pure water, *i.e.*, cases 2 and 3, respectively. In case 2, solution B was replaced by pure water after nanodroplet formation, and kept stationary. Fig. 7 shows that a large proportion of the MMA nanodroplets under these conditions dissolved within 60 min.

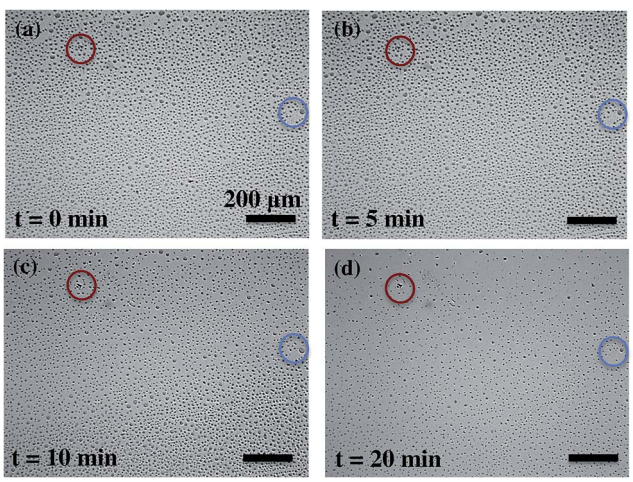

Fig. 10 Sequential optical image of HDODA nanodroplets under the flow of pure water (case 6). Many droplets disappeared in 20 min. The red and blue circles indicate the same features in four images. Length of the scale bar: 200 μm.

For these dissolving nanodroplets their lateral diameter gradually decreased with time. Three size groups are marked in red, white, and green circles in Fig. 7a. The initial size of the droplets was 5 μm (red), 8 μm (white) and 12 μm (green). The location and size of the circles in the sequential images are the same as they are in the first image. The nanodroplet shrank laterally, clearly suggesting that the three-phase contact line of droplets moved during the dissolution. Interestingly, in all cases the three-phase contact line moved only on one side, so the centre of droplet shifted as highlighted in Fig. 8. It is evident that the strength of the pinning on the three-phase contact line is not homogeneous, and the boundary moved towards the locations with the strongest pinning. The top-view of the dissolution process is sketched in Fig. 8c. It is hard to obtain ideally homogeneous surfaces under our experimental conditions. The heterogeneities are ubiquitous even on surfaces prepared with extreme caution[34,35] and lead to contact line pinning.[36,37]

Another salient feature is that nanodroplets with the same initial size did not dissolve simultaneously, but at different rates. For a given initial size of 5 μm, some of the nanodroplets had became smaller after 25 min while others completely dissolved. For the initial size of 8 μm and 12 μm, the nanodroplets became clearly smaller at the time of 30 min and 50 min, respectively, while the others completely dissolved. We trace this individuality of the surface nanodroplets back to different local pinning conditions.

MMA nanodroplets were also exposed to a slow flow of pure water (case 3). Fig. 9 shows that many of these nanodroplets had already disappeared within 9 min. The subsequent images could clearly reveal the extent of their lateral shrinkage during the dissolution. They also again revealed the individuality of the droplets. Even when similar in size, their dissolution rate varies. For instance, the nanodroplets with a 12 μm initial lateral diameter disappeared gradually in a time span between 6.6 min and 8 min. As expected, the lifetime of the nanodroplets under the slow flow of water (case 3) is considerably shorter than that under static conditions (case 2). In the latter, the water that was initially MMA free became increasingly rich in MMA as the droplets progressively dissolved, thus causing the dissolution rate to decrease with time. Since the concentration of MMA in water (*i.e.*, the undersaturation ζ) is a key parameter governing the dissolution and hence the shrinkage of the surface nanodroplets, the gradual replenishment of water under the slow flow condition allows for $c_\infty \approx 0$ and thus an undersaturation of $\zeta \approx 1$, facilitating faster droplet dissolution.

For comparison, nanodroplets comprising HDODA and decane were also exposed to the same flow of pure water (cases 6 and 9, respectively). Images of the HDODA nanodroplets obtained from the reflection mode optical microscopy in the absence of fluorescent dyes are shown in Fig. 10. Whereas some of the HDODA droplets (case 6, with a time scale about 80 times longer than that of the MMA droplets) had dissolved within 20 min, decane nanodroplets (in ESI†) did not change noticeably even after 90 min. This is due to the very low solubility of decane (see Table 1), which has by far the lowest solubility of three oils we employed, leading to a dissolution time scale $\tau(L = 10\ \mu m)$ of

 This journal is © The Royal Society of Chemistry 2015

Published on 06 January 2015. Downloaded on 03/03/2015 10:50:05.

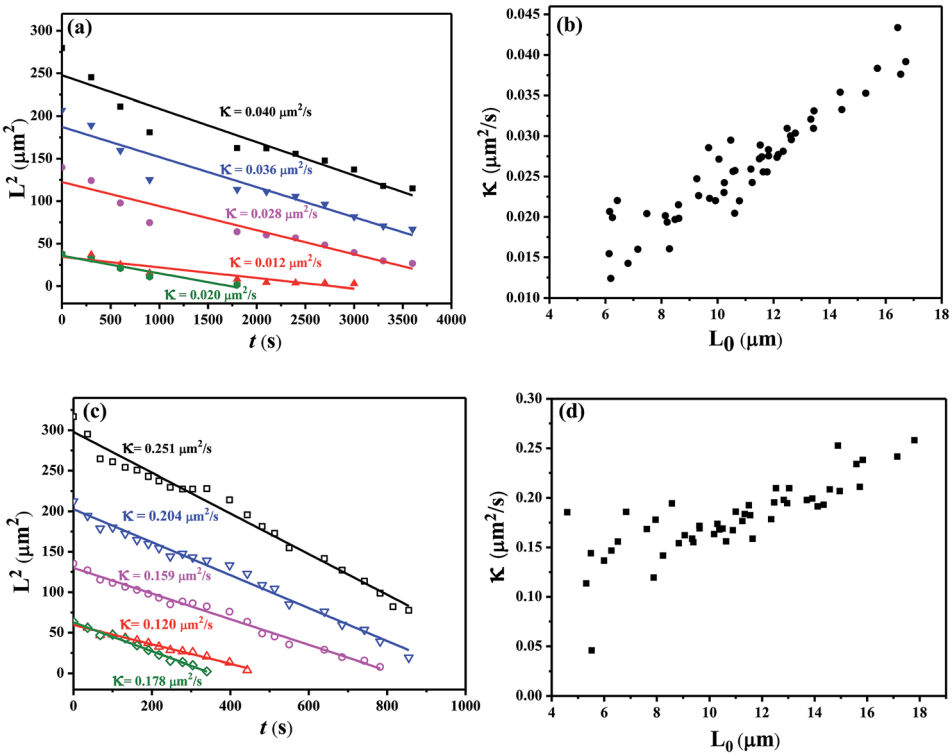

Fig. 11 Plots of the squared lateral MMA droplet diameter as a function of time for the case with initially pure water (case 2, shown in (a)) and for the case with continuously refreshing water (case 3, shown in (c)). The fluctuations in the curves presumably reflect the stick–slide behavior of the dissolving droplets. For an overall estimate, we fitted the data to a straight line, from which the dissolution rates κ for these various droplets can be determined. They are shown in (b) for the static case 2, and in (d) for the refreshing case 3. Clearly, the dissolution rates depend on the initial lateral diameter. In general, the dissolution rates for the refreshing case are larger than for the static case.

more than 20 days, much larger than that of MMA and HDODA. Clearly, given our resolution it is impossible to detect any change in size within our observation time of 1.5 hours.

Representative plots of the square of the lateral diameter as a function of time t for the MMA nanodroplets are shown in Fig. 11 under both static (case 2, Fig. 11a) and flow (case 3,

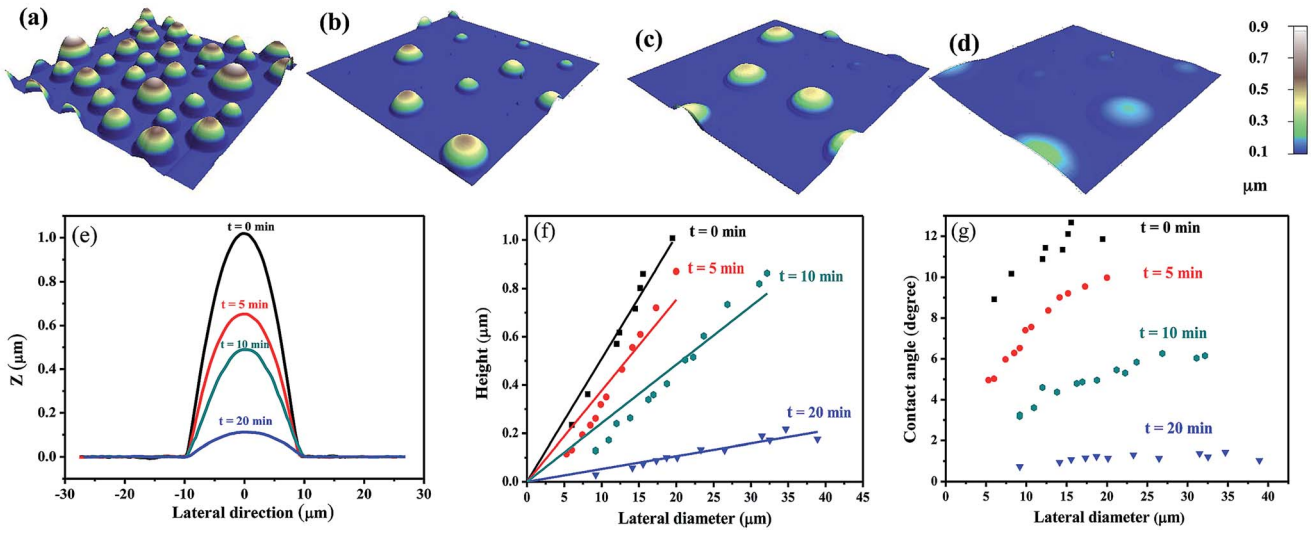

Fig. 12 Morphology of the polymerized nanodroplets. AFM images of the HDODA nanodroplets that were polymerised after dissolution in pure water flow (case 5) at (a) 0 min, (b) 5 min, (c) 10 min and (d) 20 min. The cross-sectional profiles in (e) were extracted from the images in (a)–(d) for four different polymerised nanodroplets with the same lateral diameter. From (a)–(d) the corresponding (f) height and (g) contact angle as a function of the lateral diameter were computed. The data in (f) can be barely fitted with linear lines, because the contact angles are not constant for different lateral diameters.

Published on 06 January 2015. Downloaded on 03/03/2015 10:50:05.

Fig. 11c) conditions. The dissolution curves for all the MMA nanodroplets (case 2 and 3) are provided in the ESI.† The decane droplets do not visibly shrink within our observation time, as already stated above.

Fig. 11a and c show that the square of the lateral diameter decreases approximately linearly with time as one would expect from eqn (14) for the CA mode. The typical dissolution rate κ is obtained from a linear fit to relation (14). The dissolution rates κ varied from 0.012 to 0.043 $\mu m^2\ s^{-1}$ in the static case 2, and from 0.046 to 0.258 $\mu m^2\ s^{-1}$ in the flow case. The faster dissolution in the refreshing case was to be expected as then $c_\infty \approx 0$ is reached after the initial transients. The dissolution rates κ as a function of the initial lateral diameter (L_0) are shown in Fig. 11b and d. On average, *smaller* droplets possessed *slower* dissolution rates and *vice versa*, clearly showing that the droplets do *not* dissolve in a pure CA mode.

The plots also show that the dissolution rate ($\mu m^2\ s^{-1}$) of two different nanodroplets with the *same* initial diameter of 6 μm was 0.020 $\mu m^2\ s^{-1}$ and 0.012 $\mu m^2\ s^{-1}$ in the static water. Two other droplets of both 8 μm dissolved at a rate of 0.12 $\mu m^2\ s^{-1}$ or a much higher rate of 0.18 $\mu m^2\ s^{-1}$ under the flow of water, thus confirming our previous observation that the droplets of the same size often dissolve at different rates.

We now come to the comparison of the absolute numbers of the dissolution rates with our above theoretical calculation, see Fig. 3b and 4a. Lets us first focus on the MMA droplets for which we have the most data. We see the theoretical lifetime (less than 1 s) is more than three orders of magnitude faster than the measured one (several minutes). The reason for this is that in the experiments we could not switch the MMA concentration in water to $c_\infty \approx 0$ instantaneously, *i.e.* simultaneously with the start of the droplet dissolution. The transient time during which the water with dissolved MMA could be thoroughly replaced by pure water was about two minutes. In the MMA case with its very fast dissolution timescale of less than one second the much longer duration for the changeover thus contributes significantly to the lifetime of the MMA nanodroplets.

The situation is better for HDODA droplets. As shown in Fig. 10, the time scale for HDODA droplet dissolution in pure water is on the order of 10 min, which is comparable with the theoretical timescale in Table 1. Due to their much longer theoretical lifetime as compared to MMA droplets, the duration for changeover (about two minutes) now only counts for a smaller portion of their measured lifetime and thus to better agreement. We think that an even more favourable one-to-one comparison between experiments and theory is possible for liquid droplets with much larger lifetime than the time of the transients (here about two minutes), though still not as long ones as those for the practically insoluble decane. Such quantitative studies are ongoing in our lab, but beyond the scope of the present paper, which focuses on the qualitative features of the dissolution.

3. Morphology of dissolving droplets

The contact angles of the submicron HDODA droplets were measured by polymerising them into microlenses in saturated water (case 4) to obtain the angles before the droplets start dissolving, and at different times under slowly flowing fresh water (case 6), as previously discussed in Fig. 6. Then they were AFM-imaged. The resulting AFM images shown in Fig. 12 reveal that the microlenses became progressively flatter with ongoing dissolution. For example, a droplet with an initial lateral diameter of 20 μm possessed a height of 1 μm in saturated water, which decreased to 900 nm, 400 nm, and 300 nm after 5 min, 10 min, and 20 min, respectively. The ratio of the maximum height and the lateral diameter of the nanodroplet decreased with the extent of the dissolution time. The apparent linear relationship between the height and the lateral diameter was discussed extensively in our recent work.[18]

Fig. 12g shows the corresponding contact angles across the entire range of droplet sizes. In saturated water (case 4) the contact angle of the droplets was between 8.9° and 12.8°. In the flow of pure water (case 6), the contact angle decreased to 5° to 10° and 3.2° to 6.2° after 5 min and 10 min, respectively. It further decreased to 0.7° to 1° at 20 min. The dependence of contact angles on the droplet size is seen to become less pronounced, as the range of the contact angles had become so small.

4. Dissolution mechanisms

According to eqn (14), if θ were the same for all droplets, the slope $\kappa(\theta)$ of L^2 as a function of time t should be universal for all the droplets. This, however, does not represent the dissolution of surface droplets. Instead Fig. 9d shows that the dissolution rates κ depend on the initial droplet size, indicating that the wall correction factor $f(\theta)/(3g(\theta))$ is not constant, due to the variation in θ over time. The dissolution rate was slower for the smaller droplets. This can be understood from Fig. 12g: at time zero, the droplets have a contact angle between 8° and 13°. After 10 minutes, the contact angle is between 3° and 6°, *i.e.*, smaller than even for the small droplets in the beginning. From eqn (14) and the plot in Fig. 3 of the wall correction factor $f(\theta)/(3g(\theta))$ this smaller contact angle implies a larger dissolution rate, just as seen.

The decrease of contact angle as a function of the dissolution time can exclude the scenario that the nanodroplets dissolve in a mode of constant contact angle. It seems to be that the dissolution process of surface nanodroplets is in a stick–slide mode, as sketched in Fig. 2c, where the contact area remains constant while the contact angle is decreasing from the dissolution or *vice versa*. A similar dissolution mode was also observed for dissolving nanobubbles.[13] Also a jumping-mode is possible. Strictly speaking, as we could not observe the decrease of the lateral diameter and the contact angle in parallel, we logically cannot exclude that the contact angle decreases with the three-phase contact line moving at the same time, but we consider this scenario as very unrealistic.

The droplet individuality of the dissolution rates of same-sized surface droplets can have two reasons. The first, as already mentioned above, originates from chemical or geometric surface heterogeneities, giving rise to different pinning strengths at the three phase contact line. The presence of local

 This journal is © The Royal Society of Chemistry 2015

Published on 06 January 2015. Downloaded on 03/03/2015 10:50:05.

heterogeneities is evident from the manner how the lateral diameter shrank during the dissolution. The droplet boundary moved to a side where the pinning was strongest. Nevertheless, given that droplets appeared to be mostly circular, the surface heterogeneity cannot be so strong to prevent surface tension to restore the spherical cap shape of the droplets.

An alternative mechanism for the individuality of the dissolution rate could arise from the cooperative effect between neighbouring droplets. In other words, the droplets do not dissolve independently, but crosstalk with other droplets through diffusion. Similar cooperative effects were observed and analysed for evaporating droplets.[38,39] Such cooperative effect is due to dissolving neighboring droplets which change the concentration field seen by a droplet. It thus is conceivable that each nanodroplet surrounded by others dissolves at a different rate, given that their local environment differs from that of the other droplets in the system. It is difficult to quantify the extent of such cooperative effects on the dissolution rate of individual droplets in our system, due to their polydispersity compounded by the evolution of their size and the distance with their neighbours during the dissolution. In any case, the crosstalk between the droplets is obvious.

Also the already above mentioned Ostwald ripening of some droplets is a form of cross-talk. Indeed, our results that small surface droplets became smaller or disappeared suggest the undergoing of Ostwald ripening processes in the system. Although the lateral diameter of the big droplets did not visibly increase presumably due to pinning, the height of those big droplets may have grown at expense of smaller droplets, leading to a slightly larger contact angle with time as shown in Fig. 6. On the other hand, the pinning of the three phase contact line may also slow down the Ostwald ripening, similar to the case for surface nanobubbles.[13,14] Potential approaches for future experiments to minimize the cross-talk between nanodroplets during the dissolution process would be to create nanodroplets with low number density, so that they are far apart from each other. An extremely low solubility of the droplet liquid in the surrounding liquid can also minimize the cross-talk between the droplets.

Conclusions

We show in this work that the dissolution rate of surface nanodroplets is closely related to the solubility and saturation level of the droplet phase in its surrounding liquid phase. In particular, we observed that both the lateral size and the contact angle of the surface nanodroplets decrease during the dissolution, thus suggesting that the nanodroplets shrink neither in the CA mode nor in the CR mode, but in a mixed mode. Our findings reveal that the dissolution rate is faster for droplets with larger initial sizes, although the droplets with the same initial size can dissolve at different rates, exhibiting individualism in their stability. These non-universal dissolution rates can be attributed to the local surface heterogeneity and/or cooperative effects among multiple droplets.

This work clearly also sheds light on the stability mechanism of surface nanobubbles, which we suspect to be analogous to surface nanodroplets, as the dissolution process is governed by the very same equations. In particular, we expect that the pinning on the contact line, cooperative effects from neighbouring bubbles, and the imposed initial gas concentration profile also play significant roles in the extended lifetime of nanobubbles.

Acknowledgements

X.H.Z. acknowledges the support from the Australian Research Council (FT120100473) and D.L. from an ERC-Advanced Grant. We also acknowledge Endeavor Research Fellowship, ARENA Research Fellowship and STW.

References

1 A. Mendez-Vilas, A. B. Jodar-Reyes and M. L. Gonzalez-Martin, *Small*, 2009, **5**, 1366.
2 D. Quere, *Nat. Mater.*, 2004, **3**, 79.
3 A. Ma, J. Xu, L. Yu, X. Zhang, D. Wang and H. Xu, *Chem. Commun.*, 2013, **49**, 11563.
4 T. Pompe and S. Herminghaus, *Phys. Rev. Lett.*, 2000, **85**, 1930.
5 M. A. Hampton and A. V. Nguyen, *Adv. Colloid Interface Sci.*, 2010, **154**, 30.
6 J. R. T. Seddon and D. Lohse, *J. Phys.: Condens. Matter*, 2011, **23**, 133001.
7 V. S. J. Craig, *Soft Matter*, 2011, **7**, 40.
8 N. Kameda, N. Sogoshi and S. Nakabayashi, *Surf. Sci.*, 2008, **602**, 1579.
9 J. Yang, J. Duan, D. Fornasiero and J. Ralston, *J. Phys. Chem. B*, 2003, **107**, 6139.
10 C. C. Chan and C.-D. Ohl, *Phys. Rev. Lett.*, 2012, **109**, 174501.
11 V. Belova, M. Krasowska, D. Wang, J. Ralston, D. G. Shchukin and H. Moehwald, *Chem. Sci.*, 2013, **4**, 248.
12 W. Walczyk, N. Hain and H. Schonherr, *Soft Matter*, 2014, **10**, 5945.
13 X. Zhang, D. Y. C. Chan, D. Wang and N. Maeda, *Langmuir*, 2013, **29**, 1017.
14 J. H. Weijs and D. Lohse, *Phys. Rev. Lett.*, 2013, **110**, 054501.
15 Y. Liu and X. Zhang, *J. Chem. Phys.*, 2013, **138**, 014706.
16 X. Zhang and W. Ducker, *Langmuir*, 2007, **23**, 12478.
17 X. H. Zhang, J. M. Ren, H. J. Yang, Y. H. He, J. F. Tan and G. G. Qiao, *Soft Matter*, 2012, **8**, 4314.
18 S. Peng, D. Lohse and X. Zhang, *Langmuir*, 2014, **30**, 10043.
19 S.-T. Lou, Z.-Q. Ouyang, Y. Zhang, X.-J. Li, J. Hu, M.-Q. Li and F.-J. Yang, *J. Vac. Sci. Technol., B: Microelectron. Nanometer Struct. – Process., Meas., Phenom.*, 2000, **18**, 2573.
20 X. H. Zhang, X. D. Zhang, S. T. Lou, Z. X. Zhang, J. L. Sun and J. Hu, *Langmuir*, 2004, **20**, 3813.
21 X. H. Zhang, A. Khan and W. A. Ducker, *Phys. Rev. Lett.*, 2007, **98**, 136101.
22 H. Yang, S. Peng, X. Hao, T. A. Smith, G. G. Qiao and X. Zhang, *Soft Matter*, 2014, **10**, 957.

23 R. D. Deegan, O. Bakajin, T. F. Dupont, G. Huber, S. R. Nagel and T. A. Witten, *Nature*, 1997, **389**, 827.
24 H. Hu and R. G. Larson, *J. Phys. Chem. B*, 2002, **106**, 1334.
25 Y. O. Popov, *Phys. Rev. E: Stat., Nonlinear, Soft Matter Phys.*, 2005, **71**, 036313.
26 H. Gelderblom, A. G. Marin, H. Nair, A. van Houselt, L. Lefferts, J. H. Snoeijer and D. Lohse, *Phys. Rev. E: Stat., Nonlinear, Soft Matter Phys.*, 2011, **83**, 026306.
27 R. G. Picknett and R. Bexon, *J. Colloid Interface Sci.*, 1977, **61**, 336.
28 A. G. Marin, H. Gelderblom, D. Lohse and J. H. Snoeijer, *Phys. Rev. Lett.*, 2011, **107**, 085502.
29 P. S. Epstein and M. S. Plesset, *J. Chem. Phys.*, 1950, **18**, 1505.
30 M. E. R. Shanahan, *Langmuir*, 1995, **11**, 1041.
31 J. M. Stauber, S. K. Wilson, B. R. Duffy and K. Sefiane, *J. Fluid Mech.*, 2014, **744**, R2.
32 C. Xu, S. Peng, G. O. Qiao, V. Gutowski, D. Lohse and X. Zhang, *Soft Matter*, 2014, **10**, 7857.
33 R. C. A. van der Veen, T. Tran, D. Lohse and C. Sun, *Phys. Rev. E: Stat., Nonlinear, Soft Matter Phys.*, 2012, **85**, 026315.
34 A. Checco, P. Guenoun and J. Daillant, *Phys. Rev. Lett.*, 2003, **91**, 186101.
35 A. Checco, T. Hofmann, E. DiMasi, C. T. Black and B. M. Ocko, *Nano Lett.*, 2010, **10**, 1354.
36 P. G. de Gennes, F. Brochard-Wyart, and D. Quere, *Capillarity and wetting phenomena: drops, bubbles, pearls, waves*, Springer, 2004.
37 D. Bonn, J. Eggers, J. Indekeu, J. Meunier and E. Rolley, *Rev. Mod. Phys.*, 2009, **81**, 739.
38 A. M. Lacasta, I. M. Sokolov, J. M. Sancho and F. Sagués, *Phys. Rev. E: Stat. Phys., Plasmas, Fluids, Relat. Interdiscip. Top.*, 1998, **57**, 6198.
39 P. Tolédano, B. Mettout, M. Aroyo and J. M. Perez Mato, *Phys. Rev. Lett.*, 2005, **95**, 205701.

Published on 06 January 2015. Downloaded on 03/03/2015 10:50:05.

This journal is © The Royal Society of Chemistry 2015